A 3D Polarized Reversed Monte Carlo Radiative Transfer Model for mm and sub-mm Passive Remote Sensing in Cloudy Atmospheres

Cory Davis, Claudia Emde, and Robert Harwood

***Abstract*— This paper introduces a 3D polarized radiative transfer model that has been developed to assess the influence of cirrus clouds on radiances measured by the EOS-MLS instrument. EOS-MLS is on the Aura satellite, which is due for launch in June 2004. The radiative transfer model uses a reversed Monte Carlo algorithm and has been incorporated in the ARTS 1.1.x software package. The model will be used to study aspects of the scattering problem that are not considered in the existing operational EOS-MLS cloudy-sky forward model, including the influence of non-spherical, oriented hydrometeors and 3D inhomogeneous cloud structure. This paper presents the radiative transfer algorithm and example model results, which demonstrate significant 3D and polarization effects. Although the development of this model was motivated by the EOS-MLS mission, it is also directly applicable to ground-based and down-looking geometries.**

I. Introduction

MICROWAVE limb sounding (MLS) is a powerful technique for obtaining high vertical resolution measurements of trace gases in the stratosphere and upper troposphere. The microwave region has an advantage over shorter wavelengths because measurements are less affected by liquid water clouds. However, cirrus clouds, with particle sizes often exceeding microwave wavelengths, can severely disrupt trace gas measurements. On the other hand, it is possible to obtain cloud information from MLS radiances affected by cirrus clouds. The first requirement in defining the conditions where trace gas and cloud measurements are possible is a radiative transfer model that can simulate the scattering of atmospheric thermal radiation by cirrus clouds.

The non-sphericity of cirrus particles complicates the modelling task. Cirrus clouds also have finite spatial extent and internal structure. In order to account for these possibly significant features, this study treats the problem as rigorously as possible by considering non-spherical cirrus particles and polarized 3D radiative transfer. In the past (eg. [1]), and particularly in operational retrieval software [2], excessive CPU demands have necessitated the approximations of equivalent spherical particles, and 1D radiative transfer in scattering calculations.

A survey of existing freely available radiative transfer models yielded none that were well suited to the MLS problem. For instance SHDOM [3] is unpolarised, requires particles to be spherical, and its cartesian geometry is not well-suited to the limb sounding problem. Forward Monte Carlo RT models, such as the freely available GRIMALDI [4], can be impractical for radiance measurement remote sensing applications because of the prohibitively parge number of photons required to give meaningful results for a narrow field of view.

Discrete ordinates (DOM) type methods are attractive when simulating the whole radiation field, but in the limb sounding - and other remote sensing cases, only a very limited subset of outward propagation paths are required. Also, for limb sounding simulations there is a strong variation in incoming radiance with zenith angles close to 90°. In DOM type models, this necessitates a very fine angular grid, which can be expensive.

A reversed Monte Carlo method was chosen for this study. A strong consideration here was that the simplicity of the Monte Carlo radiative transfer concept should translate to reduced development time. Also, reversed Monte Carlo methods allow all computational effort to be concentrated on calculating radiances for the desired line of sight, and the nature of Monte Carlo algorithms makes parallel computing trivial.

Among the available Backward Monte Carlo RT models, several do not allow a thermal source, or do not consider polarization fully (i.e. allowing a non-diagonal extinction matrix) (e.g. [5]), and some consider neither (e.g. [6], [7]).

A useful reference for model development in this study, is the Backward-Forward Monte Carlo (BFMC) model described by [5]. In BMFC photon paths are traced backwards from the sensor, with scattering angles and path lengths randomly chosen from probability density functions (PDF) determined by the scattering phase function, and a scalar extinction coefficient respectively. The phase matrices for every scattering event and scalar extinction are then sequentially applied to the source Stokes vector to give the Stokes vector contribution for each photon. As presented in [5], the model is only applicable to cases where the extinction matrix is diagonal - that is, where there is macroscopically isotropic and mirror-symmetric scattering media. This prompted Roberti and Kummerow [8] to abandon the Backward-Forward Monte Carlo method and choose a modified Forward Monte Carlo model. However, in this study the attractive features of Liu's Backward-Forward model are retained by utilizing importance sampling, a well known technique in Monte Carlo integration. Importance sampling allows independent variables, in this case scattering angles and path lengths, to be sampled from any distribution as long as each contribution to the final integral is properly weighted.

A radiative transfer program that includes scattering can

share several elements with a program designed for clear sky radiative transfer. These shared components include clear sky radiative transfer, management of gaseous absorption coefficients, the representation of atmospheric fields, and propagation path calculation. To take advantage of this, the scattering algorithm described in this paper was added to the existing ARTS 1-1-x software package (http://www.sat.uni-bremen.de), which is modular and easily extendible. Development time was thus considerably reduced because many of the required components were already present. ARTS-1-1-x also includes a discrete-ordinates type scattering module, described in [**?**], the performance of which will eventually be compared with that of the Monte Carlo model presented here.

II. Model

The radiative transfer model solves the vector radiative transfer equation (VRTE):

$$\frac{d\mathbf{I}(\mathbf{n})}{ds} = -\mathbf{K}(\mathbf{n})\mathbf{I}(\mathbf{n}) + \mathbf{K_a}(\mathbf{n})I_b(T) + \int_{4\pi}\mathbf{Z}(\mathbf{n},\mathbf{n}')\mathbf{I}(\mathbf{n}')d\mathbf{n}' \quad (1)$$

where $\mathbf{I}$ is the 4 element column vector of radiances $\mathbf{I} = [I,Q,U,V]^T$ with units ($\mathrm{Wm^{-2}}\mu\mathrm{m^{-1}sr^{-1}}$). This will be referred to as the Stokes vector, although normally the Stokes vector is expressed in units of intensity. s is distance along direction $\mathbf{n}$ and I_b is the Planck radiance. $\mathbf{K}(\mathbf{n})$, $\mathbf{K_a}(\mathbf{n})$, and $\mathbf{Z}(\mathbf{n},\mathbf{n}')$ are the bulk extinction matrix, absorption coefficient vector and phase matrix of the medium respectively. For brevity these have been expressed as bulk optical properties, where individual single scattering properties have been multiplied by particle number density and averaged over all orientations and particle types. The argument $\mathbf{n}$ has been retained to signify that in general these properties depend on the direction of propagation.

To apply Monte Carlo integration to the problem, the VRTE needs to be expressed in integral form. (e.g. [9])

$$\mathbf{I}(\mathbf{n},\mathbf{s_0}) = \mathbf{O}(\mathbf{u_0},\mathbf{s_0})\mathbf{I}(\mathbf{n},\mathbf{u_0}) + \int_{u_0}^{s_0}\mathbf{O}(\mathbf{s}',\mathbf{s_0})\left(\mathbf{K_a}(\mathbf{n})I_b(T) + \int_{4\pi}\mathbf{Z}(\mathbf{n},\mathbf{n}')\mathbf{I}(\mathbf{n}')d\mathbf{n}'\right)ds' \quad (2)$$

, where $\mathbf{O}(\mathbf{s}',\mathbf{s})$ is the evolution operator defined by [10]. $\mathbf{u_0}$ is the point where the line of sight intersects the far boundary of the scattering domain, and $\mathbf{s_0}$ is the exit point where the outgoing Stokes vector is calculated. In general there is no closed form expression for $\mathbf{O}(\mathbf{s}',\mathbf{s})$. However, in cases where the extinction matrix is constant along a propagation path

$$\mathbf{O}(\mathbf{s}',\mathbf{s}) = \exp\left(-\mathbf{K}\Delta s\right) \quad (3)$$

In ARTS a propagation path consists of a set of coordinates indicating where the path intersects with grid surfaces. If the extinction matrix in the path segment between two such points is considered constant, $\mathbf{K} = (\mathbf{K_j} + \mathbf{K_{j+1}})/2$, the evolution operator between two arbitrary points $\mathbf{s_0}$ and $\mathbf{s}_N$ is

$$\mathbf{O}(\mathbf{s}_0,\mathbf{s}_N) = \mathbf{O}(\mathbf{s}_{N-1},\mathbf{s}_N)\mathbf{O}(\mathbf{s}_{N-2},\mathbf{s}_{N-1})\ldots\mathbf{O}(\mathbf{s}_1,\mathbf{s}_2)\mathbf{O}(\mathbf{s}_0,\mathbf{s}_1), \quad (4)$$

, where $\mathbf{O}(\mathbf{s_i},\mathbf{s_{i+1}})$ is given by Eq. 3.

The numerical task is then to perform Monte Carlo integration on the integral on the right hand side of Eq. 2. The aim in importance sampling is to choose probability density functions (PDFs) for the independent variables that are as close as possible to being proportional to the integrand [11]. This concentrates computational effort on regions where the integrand is most significant and also reduces the variance in the contributions of each photon, thus reducing the number of photons and hence CPU time required to give a prescribed accuracy. Eq. 2 suggests that the PDF for sampling path length, where path length is the distance traced backwards from the sensor, $\Delta s = |\mathbf{s} - \mathbf{s}'|$, should be proportional in some way to the evolution operator $\mathbf{O}(\mathbf{s}',\mathbf{s})$. Likewise, new incident directions $(\theta_{inc},\phi_{inc})$ should be sampled from a PDF proportional to $\mathbf{Z}(\theta_{scat},\phi_{scat},\theta_{inc},\phi_{inc})$. Since PDFs are scalar functions, and that we consider the first element of the Stokes vector most important, we choose PDFs that are proportional to the (1,1) element of $\mathbf{O}(\mathbf{s}',\mathbf{s})$ and $\mathbf{Z}(\theta_{scat},\phi_{scat},\theta_{inc},\phi_{inc})$.

A. Algorithm

The model algorithm proceeds as follows:

1) : Begin at the cloud box exit point with a new photon. Sample a path length, Δs along the first line of sight using the PDF

$$g_0(\Delta s) = \frac{\tilde{k}\tilde{O_{11}}(\Delta s)}{1 - O_{11}(\mathbf{u_0},\mathbf{s_0})}. \quad (5)$$

, where $\tilde{O_{11}}(\Delta s)$, is the piecewise exponential function that includes $O_{11}(\mathbf{s}',\mathbf{s})$ values at points where the line of sight intersects with grid surfaces. Between two such adjacent intersections, A and B, the function $\tilde{O_{11}}(\Delta s)$ is given by

$$\tilde{O_{11}}(\Delta s) = O_{11}(\Delta s_A)\exp\left(-\tilde{k}\left(\Delta s - \Delta s_A\right)\right) \quad (6)$$

, and

$$\tilde{k} = \frac{1}{(\Delta s_B - \Delta s_A)}\ln\left(\frac{O_{11}^A}{O_{11}^B}\right) \quad (7)$$

, which, for cases where the extinction matrix is diagonal, is equal to $K_{11} = (K_{11}^A + K_{11}^B)/2$. The denominator in Eq. 5 ensures an emission or scattering event for each photon in the initial line of sight. Eq. 5 is sampled by taking a random number (from the uniform distribution [0,1]), r, and solving

$$\frac{1 - \tilde{O_{11}}(\Delta s)}{1 - O_{11}(\mathbf{u_0},\mathbf{s_0})} = r. \quad (8)$$

for Δs.

2) : Another random number, r, is drawn to choose between emission and scattering. We first define an albedo-like quantity

$$\tilde{\omega} = 1 - \frac{K_{a1}(\mathbf{n_0},\mathbf{s_1})}{K_{11}(\mathbf{n_0},\mathbf{s_1})} \quad (9)$$

Note: we can't use the actual single-scattering albedo as this depends on the polarization state of the incident radiation. If $r > \tilde{\omega}$, then the event is considered to be emission, the reversed ray tracing is terminated, and the Stokes vector contribution of the ith photon is

$$\mathbf{I^i}(\mathbf{n},\mathbf{s_0}) = \frac{\mathbf{O}(\mathbf{s_1},\mathbf{s_0})\mathbf{K_a}(\mathbf{n_0},\mathbf{s_1})I_b(T,\mathbf{s_i})}{g_0(\Delta s)\,(1-\tilde{\omega})} \quad (10)$$

, where the index i signifies photon number. Return to step 1.

Otherwise, if $r \leq \tilde{\omega}$ we have a scattering event.

3) : At the scattering point sample a new incident direction $(\theta_{inc}, \phi_{inc})$ according to

$$g(\theta_{inc}, \phi_{inc}) = \frac{Z_{11}(\theta_{scat}, \phi_{scat}, \theta_{inc}, \phi_{inc}) \sin(\theta_{inc})}{K_{11}(\theta_{scat}, \phi_{scat}) - K_{a1}(\theta_{scat}, \phi_{scat})} \quad (11)$$

, which is sampled by the rejection method as described in [11].

Calculate the matrix

$$\mathbf{Q_k} = \mathbf{Q_{k-1}} \mathbf{q_k} \quad (12)$$

, where

$$\mathbf{q_k} = \frac{\sin(\theta_{inc})_k \mathbf{O}(\mathbf{s_k}, \mathbf{s_{k-1}}) \mathbf{Z}(\mathbf{n_{k-1}}, \mathbf{n_k})}{g\left(\Delta s\right) g(\theta_{inc}, \phi_{inc}) \tilde{\omega}}, \quad (13)$$

and $\mathbf{Q_0} = \mathbb{1}$. The index k represents the scattering order.

4) : Choose a path length along the new direction according to

$$g(\Delta s) = \tilde{k} \tilde{O_{11}}(\Delta s) \quad (14)$$

This is sampled by taking a random number and solving

$$\tilde{O_{11}}(\Delta s) = r. \quad (15)$$

for Δs. If $r < O_{11}(\mathbf{u_k}, \mathbf{s_k})$, where $\mathbf{u}_k$ is the boundary of the scattering domain in the current line of sight, the photon leaves the scattering domain, and the contribution for photon i is

$$\mathbf{I^i}(\mathbf{n}, \mathbf{s_0}) = \frac{\mathbf{Q_k} \mathbf{O}(\mathbf{u_k}, \mathbf{s_k}) \mathbf{I}(\mathbf{n_k}, \mathbf{u_k})}{O_{11}(\mathbf{u_k}, \mathbf{s_k})} \quad (16)$$

, where $\mathbf{I}(\mathbf{n_k}, \mathbf{u_k})$ is the incoming radiance at $\mathbf{u}_k$. This is calculated with the standard ARTS clear-sky routine. Return to step 1.

Otherwise, if the sampled path length keeps the path within the scattering domain...

5) : As in step 2, calculate $\tilde{\omega}$ at the new point, $\mathbf{s_{k+1}}$, and draw a uniform random deviate, r.

If $r > \tilde{\omega}$, then the event is considered to be emission, the reversed ray tracing is terminated, the Stokes vector contribution is

$$\mathbf{I^i}(\mathbf{n}, \mathbf{s_0}) = \frac{\mathbf{Q_k} \mathbf{O}(\mathbf{s_{k+1}}, \mathbf{s_k}) \mathbf{K_a}(\mathbf{n_k}, \mathbf{s_{k+1}}) I_b(T, \mathbf{s_{k+1}})}{g\left(\Delta s\right)\left(1 - \tilde{\omega}\right)} \quad (17)$$

, and we return to step 1.

Otherwise, if $r \leq \tilde{\omega}$ we have a scattering event and we return to step 3.

6) : Once the prescribed number, N, of photon contributions, $\mathbf{I^i}(\mathbf{n}, \mathbf{s_0})$, have been calculated, the cloud box exit Stokes vector is given by

$$\mathbf{I}(\mathbf{n}, \mathbf{s_0}) = \mathbf{O}(\mathbf{u_0}, \mathbf{s_0}) \mathbf{I}(\mathbf{n}, \mathbf{u_0}) + \langle \mathbf{I^i}(\mathbf{n}, \mathbf{s_0}) \rangle. \quad (18)$$

, with an estimated error for each Stokes index, j, of

$$\delta I_j = \sqrt{\frac{\langle I_j^2 \rangle - \langle I_j \rangle^2}{N}}. \quad (19)$$

When simulating an MLS measurement, an extra clear sky RT calculation is performed from the cloud box exit to the sensor, with the Monte Carlo result from Eq. 18 taken as the radiative background.

B. Software implementation

The above algorithm is contained within a module that has been added to the Atmospheric Radiative Transfer Simulator (ARTS) 1.1.x software package, which is being developed at several European Institutes. The software is written in C++ and is available under the Gnu General Public License. Some brief notes follow regarding details of the software implementation of the algorithm described above.

Atmospheric grids: In ARTS the atmosphere is gridded by latitude, longitude and pressure coordinates. Because radiative transfer calculations with scattering are generally much more expensive than clear sky radiative transfer, scattering calculations are confined to a sub-domain of the modelled atmosphere called the *cloud box*.

Scattering Properties: In this study we consider spheroidal and cylindrical ice particles, with both completely random orientation or horizontally alignment with random azimuthal orientation. The single scattering properties for these particles is obtained software derived from the random [12] and fixed [13] T-matrix codes of Mishchenko. Because of the computational expense of the T-matrix calculations, single scattering properties are precalculated, imported in XML format, and interpolated as required. The complex refractive index of ice is obtained from the tabulated data of Warren[14].

Random number generation: Random numbers for path length and direction sampling are generated using the MT19937 generator of Matsumoto and Nishimura [15] as implemented in the GNU Scientific Library (http://www.gnu.org/software/gsl/).

Parallelization: The nature of the Monte Carlo algorithm makes utilization of multiple processors for single simulations trivial. The most straightforward method is to divide the desired number of photons among available processors and combine the results.

III. Example Results

Some example model output is shown in Fig. 2. The example atmospheric scenario was constructed by taking a 1D profile of ice water content (IWC), temperature, and gas species mixing ratios from an MLS simulated data swath that has been used for EOS-MLS retrieval algorithm development. The 1-D IWC profile was then superimposed on 3-D cloud shape resembling a tropical cumulonimbus anvil. Fig. 1 illustrates the cloud scenario, and also shows the lines of sight used in the radiative transfer simulations. The correlation of McFarquhar and Heymsfield [16] was used to obtain particle size distributions corresponding to IWC and temperature. This distribution was divided into 40 size bins for the calculation of single scattering properties. Results are shown for 3 particle types: spheres, prolate spheroids (aspect ratio = 0.5), and oblate cylinders (aspect ratio = 2). Particle sizes are binned on an equal volume basis to conserve IWC. The blue curves in Fig. 2 are for horizontally aligned prolate spheroids; the particle rotation axes have a zenith angle of 90° and have a random azimuthal orientation angle. The cyan curves are for the same particles but with completely random orientation. The red curves are for horizontally aligned oblate cylinders, where

the axes of rotation are parallel with the local zenith. These different microphysical scenarios were selected to demonstrate the model's capability rather than to accurately reflect an actual cirrus cloud.

The frequency considered here, 200.5 GHz, is in the upper side-band of Band 2 on Radiometer 2 of the EOS-MLS instrument. In these tests two sets of viewing directions, labelled A and B in Fig. 1, are considered. Both sets consider the same tangent heights, $6.5km \leq z_{tan} \leq 13.5km$, but have a different scheme for placing the sensor relative to the cloud. In set A the sensor is positioned so that the tangent point lies within the cloud, at (0N,0E). In set B each line of sight passes through (0N,-0.5E, 13.5km), so that the tangent point is either in or behind the cloud when viewed from the sensor.

In these simulations the cloudbox was determined from the extent of the cloud shown in Fig. 2, and was discretized on a $20 \times 20 \times 20$ grid. This grid was then merged with a $100 \times 100 \times 100$ grid spanning the modelled atmosphere to give a combined $120 \times 120 \times 120$ grid. The modelled atmosphere must be large enough so that no propagation path can enter the cloud box from a point on any side boundry of the modelled atmosphere.

For each simulation 4×10^5 photons were used. Each simulation was run on a single 2.8 GHz CPU.

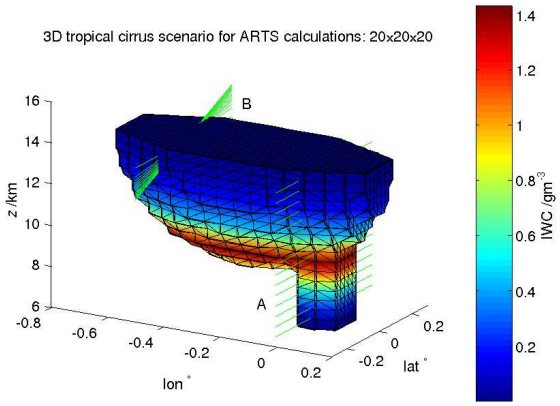

Fig. 1. 3D cloud scenario for example results

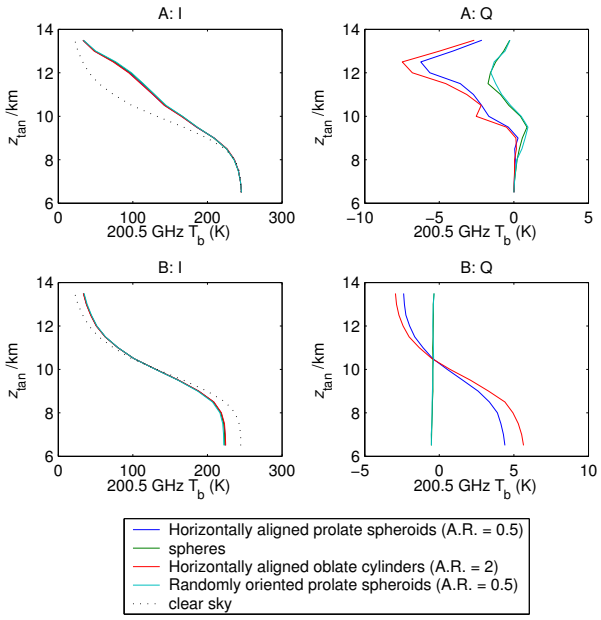

Fig. 2. Simulated single sideband EOSMLS radiances, I, and polarization differences, $Q = I_v - I_h$, for 200.5 GHZ. The cloud scenario for these simulations is shown in Fig. 1

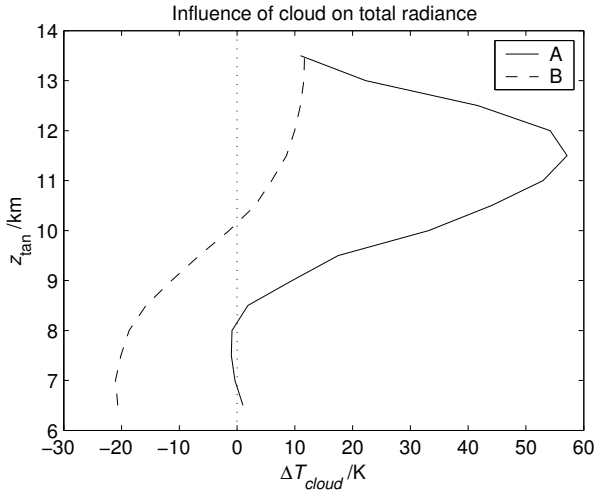

Fig. 3. The incluence of the cloudy scenario in Fig. 1 (with horizontally aligned prolate spheroids) on the total radiance, $\Delta T_{cloud} = I_{cloudy} - I_{clear}$, for viewing direction sets A and B.

A. Results

Fig. 2 shows values fo the total radiance, $I = I_v + I_h$, and polarization difference, $Q = I_v - I_h$, for the simulations described above. Both quantities are expressed as Rayleigh-Jean brightness temperature. The other Stokes elements, U and V, are not shown as their magnitude is insignifant in comparison with I and Q. Moreover, the EOS-MLS antennas only measure horizontal and vertical polarizations. The top row of plots are for viewing direction set A and the bottom row is for set B.

The first column of plots in Fig. 2 indicates that the choice of particle type and orientation scheme had little effect on the total radiance. However, particle type, and orientation did have a significant impact on the polarization difference. Although randomly oriented prolate spheroids behaved almost exactly like spherical particles (of the same volume), the horizontally aligned prolate spheroids and oblate cylinders gave significant partial horizontal or vertical polarization - depending on the viewing direction. For simulation set A, the horizontally aligned particles gave partial horizontal polarization for tangent heights above 9 km. For simulation set B, the horizontally aligned particles gave partial horizontal polarization for tangent heights above 10.5 km but partial vertical polarization for tangent heights below 10.5 km. The sign of the polarization signal is determined by the magnitude of two opposing mechanisms: dichroism, as manifest by a non-diagonal extinction matrix, $\mathbf{K}$; and the effect of radiation

being scattered into the line of sight. In the cases presented here the horizontally aligned non-spherical particles have a negative K_{21}, which has the effect of vertically polarizing radiation. The magnitude of this effect on the measured radiance depends on the source radiance. The contribution to the polarization signal of radiation scattered into the line of sight depends on both the spatial distribution of incoming radiance, and the shape and orientation of scattering particles, which, in the case of horizontally aligned particles contributes to horizontal polarization. The mechanisms above combine to give the different Q profiles for cases A and B. In both cases for high tangent heights the radiative background is cold so that the dichroism effect is small in comparison with the scattering integral contribution. This yields the partial horizontal polarization (negative Q) at high tangent heights; Q is more negative in case A because of the greater pathlength within the cloud, and for a given tangent height the path in case A traverses a warmer part of the cloud, thus increasing the scattering integral contribution. The warmer source radiance at low tangent heights increases the dichroism effect - giving positive Q in case B. Case A does not exhibit positive Q at low tangent heights because of the dominance of gaseous emission and absorption between the cloud and the sensor.

Cases A and B also produce significantly different radiance profiles, as demonstrated in the first column of Fig. 2. This difference is clarified by Fig. 3, where the difference between cloudy sky and clear sky radiance, $\Delta T_{cloud} = I_{cloudy} - I_{clear}$, is plotted for cases A and B with the cloud composed of horizontally aligned prolate spheroids. In both cases there is a positive ΔT_{cloud} for high tangent heights due to the scattering of warm radiances into the line of sight; the effect is greater in case A due to the increased length and decreased altitude of the in-cloud optical path. At low tangent heights in case B the cloud has a negative impact on the simulated radiance; this is not observed in case A due to the placement of the tangent point within the cloud, and the dominance of gaseous emission and absorption between the cloud and the sensor.

B. Performance

Fig. 4 shows the estimated error in the first two elements of the cloudbox exit Stokes vector for all of the example simulations. These were obtained from the Monte Carlo algorithm by Eq. 19. To get an estimate of the error of the simulated measured radiance, these values must be multiplied by the clear sky transmittance between the cloudbox and the sensor. These plots show that the estimated error in cloudbox exit Stokes vector is strongly dependent on the optical thickness in the line of sight, and relatively independent of particle type and orientation.

Although the absolute error in polarization difference is generally lower than that for total radiance, the relative error is much higher. This is apparent in the top right panel of Fig. 2, where some noise is evident at intermediate tangent heights, where cloudbox exit Stokes vector error is largest. Therefore in some cases, where accurate Q determination is desired, it may be necessary to increase the number of photons used in the simulation.

The 2nd column of plots in Fig. 4 show the time taken for each simulation. These values obviously depend on a range of factors to do with the computing environment and compilation options. However, the plots do demonstrate that CPU time, like cloudbox exit Stokes vector error is strongly dependent on ice water path and the IWC of the scattering domain. Also, the calculations involving horizontally aligned particles were considerably more expensive than those for spheres or randomly oriented particles. This reflects the additional cost of non-diagonal extinction matrices and the extra angular dependencies of optical properties for horizontally aligned particles.

Memory use for each of the example simulations was 300MB or less.

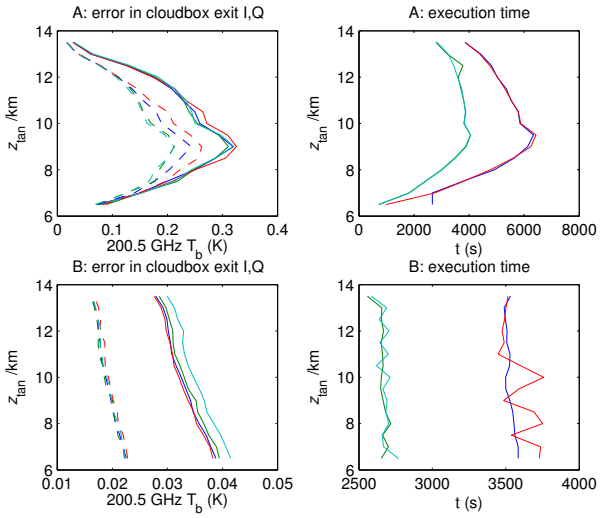

Fig. 4. Estimated error in cloudbox exit radiance (solid) and polarization difference (dashed) for the simulations presented above. Line colours are as in Fig. 2 The right column shows the execution time for each simulation.

IV. Discussion and Future Work

A reversed Monte Carlo algorithm has been presented for 3D polarized transfer in mm and sub-mm remote sensing applications. Although 3D polarized radiative transfer calculations are computationally demanding, the example limb sounding simulations shown in this paper demonstrate that the software implementation of the algorithm provides acceptable accuracy, and execution times that are practical for use in research. Like the rest of the ARTS package, this software is freely available under the Gnu General Public License, and can be downloaded from http://www.sat.uni-bremen.de.

Although the example simulations presented here are only intended to illustrate the capabilities of the radiative transfer model, the results suggest that it is important to consider more than one spatial dimension and also polarization when simulating microwave limb sounding measurements. The different particle and viewing direction schemes used in section III would all have the same representation in a 1-D model that uses equivalent spheres, so the variation in Stokes vector profiles shown in Fig. 2 would be missed.

It is planned to use the model presented here to study the influence of cirrus microphysics and macroscopic structure on EOS-MLS radiances. It is hoped that this work will increase the amount and quality of cloud information retrieved by EOS-MLS. Although the scattering model was developed with microwave limb sounding in mind, it is also directly applicable to other viewing geometries.

V. Acknowledgments

The first author wishes to acknowledge the developers of ARTS for providing such a useful platform. In particular, thanks are due to Stefan Bühler, Patrick Eriksson, Sreerekha Ravi, and Oliver Lemke for helpful advice on including the Monte Carlo algorithm in ARTS. Thanks are also due to Jonathan Jiang at JPL for helpful discussions and model comparisons.

The first author is funded by NERC as part of the Clouds Water Vapour and Climate thematic programme.

References

[1] S. T. Bond, "The potential effect of cirrus on microwave limb sounder retrievals," Ph.D. dissertation, University of Edinburgh, 1996.
[2] D. L. Wu and J. H. Jiang, "Eos mls algorithm theoretical basis for cloud measurements," Jet Propulsion Loboratory, Tech. Rep., 2002.
[3] K. F. Evans, "The spherical harmonics discrete ordinate method for three-dimensional atmospheric radiative transfer," *Journal of the Atmospheric Sciences*, vol. 55, pp. 429–446, 1998.
[4] A. Macke, D. L. Mitchell, and L. V. Bremen, "Monte carlo radiative transfer calculations for inhomogeneous mixed phase clouds," *Phys. Chem. Earth (B)*, vol. 24, no. 3, pp. 237–241, 1999.
[5] Q. Liu, C. Simmer, and E. Ruprecht, "Three-dimensional radiative transfer effects of clouds in the microwave spectral range," *Journal of Geophysical Research*, vol. 101, no. D2, pp. 4289–4298, 1996.
[6] E. Oikarinen, L.and Sihvola and E. Kyrola, "Multiple scattering radiance in limb-viewing geometry," *J. Geophys. Res.*, vol. 104, no. D24, pp. 31 261–31 274, 1999.
[7] K. Ishimoto, H.and Masuda, "A monte carlo approach for the calculation of polarized light: application to an incident narrow beam," *J. Quant. Spectrosc. Radiat. Transf.*, vol. 72, no. 4, pp. 462–483, 2002.
[8] L. Roberti and C. Kummerow, "Monte carlo calculations of polarized microwave radiation emerging from cloud structures," *J. Geophys. Res.*, vol. 104, no. D2, pp. 2093–2104, 1999.
[9] H. Hochstadt, *Differential Equations: A Modern Approach*. Holt, Rinehart, and Winston, 1964.
[10] E. L. Degl'Innocenti and M. L. Degl'Innocenti, *Solar Physics*, vol. 97, p. 239, 1985.
[11] J. Liu, *Monte Carlo Strategies in Scientific Computing*. Springer-Verlag, 2001.
[12] M. Mishchenko and L. Travis, "Capabilities and limitations of a current FORTRAN implementation of the T-matrix method for randomly oriented, rotationally symmetric scatterers," *J. Quant. Spectrosc. Radiat. Transfer*, vol. 60, no. 3, pp. 309–324, 1998.
[13] M. Mishchenko, "Calculation of the amplitude matrix for a nonspherical particle in a fixed orientation," *Applied Optics*, vol. 39, no. 6, pp. 1026–1031, 2000.
[14] S. Warren, "Optical constants of ice from the ultraviolet to the microwave," *Applied Optics*, vol. 23, no. 8, pp. 1206–1225, 1984.
[15] M. Matsumoto and T. Nishimura, "Mersenne twister: A 623-dimensionally equidistributed uniform pseudorandom number generator," *ACM Transactions on Modeling and Computer Simulation*, vol. 8, pp. 3–30, 1998.
[16] G. McFarquhar and A. Heymsfield, "Parametrization of tropical ice crystal size distributions and implications for radiative transfer: Results from cepex," *J. Atmos. Sci.*, vol. 54, pp. 2187–2200, 1997.

Cory Davis Cory Davis recieved the degrees of BSc (Hons,1) and Ph. D. in physics at the University of Otago, Dunedin, New Zealand, in 1996 and 2001 respectively. Currently he is a post-doctoral research fellow the Institute for Atmospheric and Environmental Science at the University of Edinburgh, Scotland. Dr. Davis is a member of the Microwave Limb Sounding team at this institute, and is funded under the NERC Clouds, Water Vapour and Climate (CWVC) thematic program. His primarily research interest is the influence of Cirrus on EOS-MLS trace gas and cloud property retrievals.

PLACE PHOTO HERE

Claudia Emde Claudia Emde received the diploma degree in Physics at the University of Bremen, Germany, in 2001. Currently she works as a PhD student in the Institute of Environmental Physics at the same University. C. Emde is a member of the Satellite Microwave Atmospheric Sounding Group and she is funded by the German Federal Ministry of Education and Research (BMBF), within the DLR project SMILES, grant 50 EE 9815. Her research interest is radiative transfer modeling to study the impact of cirrus clouds on microwave radiation in the atmosphere.

Robert Harwood Bobs biography